DOI: 10.13009/EUCASS2022-6085
9TH EUROPEAN CONFERENCE FOR AERONAUTICS AND SPACE SCIENCES (EUCASS)

Flow separation and wake of a transport aircraft configuration at beginning stall

Maximilian EHRLE*, Thorsten LUTZ* and Ewald KRÄMER*
University of Stuttgart, Faculty 6: Aerospace Engineering and Geodesy, Institute of Aerodynamics and Gas Dynamics, Pfaffenwaldring 21, 70569 Stuttgart, Germany, {ehrle,lutz,kraemer}@iag.uni-stuttgart.de

Abstract

In the present work, hybrid RANS/LES simulations of the NASA Common Research Model at the onset of stall are presented. The simulations were validated against experimental data from cryogenic measurements in the European Transonic Windtunnel within the European ESWI^{RP} project. It was shown that the simulation setup is capable of reproducing the stall on the swept wing of a transport aircraft configuration. The analysis of the stall characteristics and the wake at two angles of attack provided information about the flow physics occurring. In the spanwise direction, the wake exhibits an undulating shape resulting from two streamwise vortices. The first vortex originates from the wing tip, the second vortex limits the area of separated flow inboard where it detaches from the wing surface. With increasing angle of attack, the latter moves inboard and the separation region increases in size. The turbulence above the wing and in the wake is driven by the leading and trailing edge shear layers that bread up and consequently interact in the wake, which leads to a large-scale vortex shedding.

1. Introduction

In order to characterize the behavior of passenger aircraft beyond the limits of the flight envelope, an understanding of the occurring flow physics is crucial. Predictions of the stalling characteristics of the wing, including the formation of vortices and turbulent structures, as well as their propagation in the wake, are essential for structural integrity and control. Since such conditions, far from the design point, are difficult to predict via wind tunnel experiments or flight tests, reliable simulation methods are key to these studies.
Investigations of the post stall at high angles of attack in the authors' working group showed that scale resolving approaches are mandatory for the prediction of the wake evolution and the flow physics in the wake of the NASA Common Research Model (CRM) [1,2]. In these flow conditions, the use of hybrid RANS/LES (Reynolds averaged Navier-Stokes / Large Eddy Simulation) methods is facilitated because the separation is triggered directly at the leading edge of the wing by the geometric shape and extends over the entire wing span.
As wing stall already begins at moderate angles of attack at the investigated Mach numbers, this region of the polar curve must be considered if the stall behavior is to be understood over the entire α-range. Such conditions introduce variable separation position, varying spanwise stall characteristics, or transient reattachment phenomena. These additional difficulties pose a significant challenge for numerical methods to properly predict the correct angle of attack at which stall occurs, the separation position and the development of separation induced turbulence.
Complementary to the preliminary work in the authors' working group [1,2], the present investigation focuses on the flow around the NASA Common Research Model (CRM) in cruise configuration at beginning stall and flight relevant Reynolds numbers. The simulations are performed with the hybrid RANS/LES model BDES [16], which provides a robust boundary layer shielding under these challenging flow conditions.
Surface pressure measurements from the ESWI^{RP} project [3] are compared to the simulations for the validation of the starting conditions of the turbulent wake. Subsequently, investigations of the flow physics in the separated wake of the wing are presented at two angles of attack. The overall objective of this work is to gain a better understanding of the stall characteristics and wake downstream of flow separation regions on a swept wing typical of transport aircraft at beginning stall.

1.1. Flow Separation and Wake Flows of Swept Wings

The CRM [4], which is investigated in the following, has established itself as a widely used configuration for studies focusing on contemporary aircraft designs. Within the scope of numerical investigations at a flight relevant Reynolds

DOI: 10.13009/EUCASS2022-6085

number of 11.2Mio [3] and a Mach number of 0.25 it was possible to observe flow separation beginning at an angle of attack of 10° at the wing tip, which expands over the entire wing as the angle of attack increases. Low speed stall at high angles of attack at the CRM has been extensively studied by Waldmann et al.[1,2]. They showed that the post-stall wake is dominated by the shear layers emanating from the leading edge and trailing edge of the wing, whose destabilization and collapse determine the shape and size of the recirculation region. The wake structures revealed a bluff body like behavior, with a large wake undulating in the manner of a Kármán vortex street. The non-dimensional frequency based on the projection of the body to a plane normal to the inflow direction of this dominant wake motion was in the order of Sr_d =0.2. This agrees with the values of Huang and Lin [7] obtained for unswept airfoils with what they referred to as supercritical regime. Consequently, it could be shown that the chosen numerical setup enables insight into the occurring flow physics and wake dynamics.
Harper and Maki [6] discussed the stall characteristics of swept wings and showed that wing sweep might result in a shift of flow separation from the trailing edge to the leading edge and to the wing tip. On highly swept wings, the roll-up of vortices originating from the leading edge induces additional, nonlinear lift. At high angles of attack a vortex aligned with the leading edge may also occur at moderately swept wings typical for airliners. Polhamus [7] connected the formation of this vortex with the spanwise pressure gradient induced by wing sweep. Increasing angle of attack can lead to a detachment of the vortex from the leading edge combined with a backward curvature toward the wing tip. The measurements of Zhang et al. [8] confirmed this behavior and showed that the point, where the vortical structure detaches from the leading edge and leaves the surface moves inboard with increasing angle of attack. This flow characteristic with flow separation being induced by a vortical structure departing from the wing surface was also shown by Ehrle et al. [9] at the CRM. They showed that flow separation starts at the leading edge in the outboard wing area and shifts inboard with increasing angle of attack. Moreover, they stated that the leading edge stall behavior might be also amplified by the characteristic strong suction peak of transonic airfoils such as the one used at the CRM.

1.2. Hybrid RANS/LES Models

Hybrid RANS/LES approaches allow the scale resolving simulation of turbulence without the high computational costs of a wall-resolved LES. This is enabled by predicting the boundary layer flow with common RANS models and switching to LES mode in areas further away from the surface. Nevertheless, these models have two main issues, namely model stress depletion (MSD) which may lead to grid induced separation (GIS) and the so called "gray area problem".
MSD and GIS are major problems when pressure induced flow separation without geometrically triggered separation position occurs. At such conditions the model may switch too early to LES mode already inside the attached boundary layer, which results in premature flow separation. To tackle this problem, several shielding functions have been developed to protect the boundary layer from the intrusion of LES content. Among others, the common shielding functions of the DDES [10] and the IDDES [11] models are widely used. However, these popular hybrid RANS/LES models still show weaknesses when pressure induced flow separation without clearly defined separation position occurs. In this case, grid refinement might lead to a breakdown of the shielding functions [12].

The gray area problem generally occurs at the interface between RANS and LES zones where resolved turbulence needs some time and distance to develop when switching to LES mode. This may cause e.g. non-physical stabilization of shear layers and therefore deteriorates the numerical results. Reducing the artificial dissipation to a minimum has proven to effectively reduce the gray area as shown by Waldmann et al. at the CRM [2]. Furthermore, specific gray area mitigation tools have been subject of numerous research. Mockett et al. [13] presented a modified filter width model which considers the local flow vorticity and aligns the filter width as the maximum cell width perpendicular to the effective vorticity axis. This reduces the filter width in regions, with maximum cell spacing along the vorticity axis. Further modifications of the filter width were performed by Shur et al.[14] who added a shear layer sensor to the model of Mockett et al.[13]. This shear layer adaptive filter width model (Δ_{SLA}) reduces the filter width in shear layers in order to unlock the resolution of Kelvin-Helmholtz (KH) instabilities and accelerates the shear layer breakup. However, this model drastically reduces the eddy viscosity level when switching from RANS to LES mode and therefore might lead to the breakdown of eddy viscosity dependent shielding functions such as the one used in DDES.

At high angles of attack in post stall conditions, such as investigated by Waldmann et al.[1,2] the separation is geometrically triggered directly at the wing leading edge and extends over the entire wing span. This facilitates the use of DES-type methods as no attached boundary layer has to be shielded in these regions. They demonstrated good agreement of DDES simulation results with experimental data for high angles of attack leading to reliable results for the prediction of aerodynamic coefficients. However, in the α-range between separation onset and full stall conditions, the separation location may vary. Attached boundary layers undergoing adverse pressure gradients on the wing suction side require a robust shielding against the intrusion of LES content. In addition, spanwise flow effects on

DOI: 10.13009/EUCASS2022-6085

swept wings may lead to variations of separation characteristics or possible unsteady reattachment phenomena that make a proper representation of the flow physics even more difficult. Ehrle et al.[9] showed that IDDES, DDES and the applied AZDES method [15] have shortcomings when dealing with the present case of incipient flow separation. When applying IDDES, grid induced separation occurs at the inboard portion of the wing. DDES and AZDES were able to shield the boundary layer. However, a further refinement of the spanwise grid spacing also lead to GIS in case of the DDES model. AZDES, a zonal method, is able to successfully shield the boundary layer. However, the chosen RANS zones are thicker, which increases the gray area problem and delays the formation of resolved turbulence.
The BDES model of Weihing et al. [16] introduces a shielding function based on the Bernoulli principle. An inviscid reference state is calculated at each point in the flow field starting from the known free stream flow conditions by applying the isentropic relation and evaluating the local pressure. Consequently, the boundary layer edge is determined from the comparison of the local velocity with the inviscid reference velocity by applying the common δ_{99} criterion for the boundary layer edge velocity. This follows the main idea that energy from the flow is only extracted in the boundary layers. Consequently, the local velocity is lower in the boundary layers than the inviscid reference velocity. Investigations of pressure induced stall at a NACA $64_{(3)}$-418 airfoil by Weihing et al.[16] showed robust shielding at these conditions.
The preliminary studies [9] and investigations of different gray area mitigation tools in the preparation of the present work indicate that when the separated shear layer emanating drom the leading edge moves from RANS to LES domains, its breakdown is delayed due to the gray area. This was identified as one main driver for the overestimation of flow separation at beginning stall. A too stable shear layer leads to an increased inboard shift of the inner vortex, which triggers separation outboard from the vortex position. Furthermore, this delay influences the turbulence downstream in the wake.
All in all, hybrid RANS/LES models enable a more accurate representation of the turbulence in regions of separated flow compared to RANS approaches. However, for an accurate prediction of the separation position and the development of resolved turbulence, the boundary layer has to be sufficiently shielded and the gray area effectively mitigated. Both measures are crucial for the investigation of the size and shape of the recirculation region above the wing and therefore for the starting conditions of the separated wake.

2. Simulation Setup

The flow conditions of the numerical investigations in the present work are listed in Table 1. They are chosen according to run 316 of the ESWI^{RP} wind tunnel measurements in the European Transonic Windtunnel (ETW) [3]. A 2.7% scale model of the NASA CRM [4] was used in the wind tunnel campaign and the simulations accordingly resulting in a mean aerodynamic chord (MAC) of 0.189m. The angles of attack on which this work focuses are 12° and 14°.

Table 1: Inflow conditions

M_∞	Re_∞	α
0.25	$11.6 \cdot 10^6$	$12°, 14°$

The TAU code [17] version 2018.1.0 developed by DLR was used for the simulations in the present work. The unstructured finite volume solver TAU achieves second order accuracy in space and time by applying a central differencing scheme for the convective terms and a backward Euler dual time stepping scheme, respectively. The convective fluxes of the turbulence equations are solved using a first order Roe scheme, the linear solver applies a lower-upper symmetric Gauss-Seidel (LU-SGS) scheme. A physical timestep of 100 timesteps per convective time scale $t_\infty = MAC/u_\infty$ is chosen according to Waldmann et al. [1], which corresponds to Δt=34μs and results in a convective CFL number between 1 and 2 in the regions of separated flow. Following the guidelines of Spalart [18] this is sufficient for resolving the major turbulent scales in the separated wake. Convergence acceleration is realized via a 5w multigrid cycle. The number of inner iterations is set to 100. Numerical errors are reduced by employing the low dissipation and low dispersion model [19] in LES regions. This is enabled by a spatial blending based on the work of [20] that enables different dissipation and dispersion settings in RANS and LES areas of the hybrid RANS/LES model. Matrix valued dissipation with $k^{(4)}$=1/1024 is chosen in LES regions whereas $k^{(4)}$ is set to 1/128 in RANS regions to stabilize the numerical scheme. As a measure to improve the mitigation of the gray area problem of hybrid RANS/LES-models, the shear layer adaptive filter width model Δ_{SLA} according to [14] is applied.
The one-equation Spalart-Allmaras (SA) turbulence model [21] is used as background model for the hybrid RANS/LES simulation. The employed model version corresponds to the original model presented by Spalart and does not include the f_t and f_{t2} terms in this implementation. As a consequence of the high Reynolds number and the high angles of

DOI: 10.13009/EUCASS2022-6085

attack with a strong suction peak associated with adverse pressure gradient, the flow is considered fully turbulent in the simulations.
A ramp up of the angle of attack until the desired α-value is performed with steady state simulations as starting point for unsteady URANS simulations. The hybrid simulations are subsequently based on these unsteady RANS results. After an initial simulation period of 25 convective times in order to ensure statistical convergence, the statistics in the present work are extracted over 100 convective times.

2.1. Computational Mesh

The computational grid shown in Figure 1 corresponds to the hybrid grid described in detail by Waldmann et al. [1] with fully structured surface mesh on the wing suction side and the structured mesh above the wing and in the wake ranging over the entire wing span. Furthermore, the spanwise resolution was refined and the wind tunnel mounting additionally included. As shown by Ehrle et al.[22] the wind tunnel mounting influences the flow near the fuselage and in the wake. Therefore, an improved prediction of the wake position is expected when considering the mounting sting.
A half model of the CRM with symmetry boundary conditions embedded into a semi spherical farfield is used for the simulations. A triangular surface mesh is used on the fuselage and a fully structured mesh on the wing and tailplane surfaces resulting in prisms and hexahedra in the boundary layer regions. The mesh resolution on the wall is chosen in such a way that y^+ of the first gridpoint is smaller than one on the entire airplane surface.
In the wake region a fully structured mesh block with nearly isotropic cells is inserted, which ranges downstream behind the horizontal tailplane. The characteristic grid spacing in this region is 1%MAC.
The deformation of the wind tunnel model was considered by deforming the wing according to the deformations measured during the wind tunnel campaign, as shown by Lutz et al. [3]. The mesh topology is shown in Figure 1, with a slice though the structured block on the wing suction side colored in blue. Overall, the grid contains a total of 120 million gridpoints.
The simulation uses an aircraft fixed coordinate system with the origin located upstream of the aircraft nose, the x-axis aligned with the fuselage, the y-axis in spanwise and the z-axis in transeverse direction. For the flow investigations, a wind tunnel fixed coordinate system is used, where the origin is located at the point of rotation of the wind tunnel model, located in the fuselage center above the wing. To obtain the coordinate systems at different angles of attack, the origin of the airplane fixed coordinate system is translated to this point and consequently the entire model and flow field is rotated around the y-axis by the respective α value.

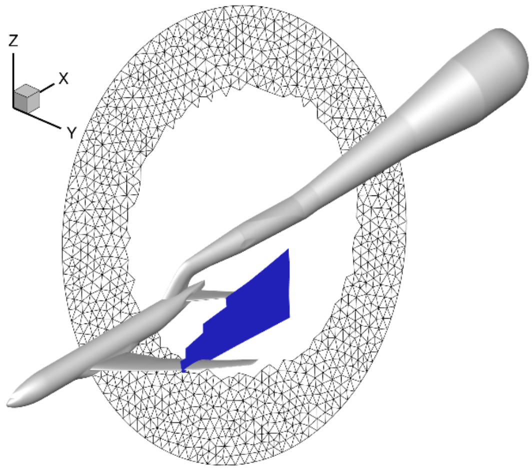

Figure 1: Topology of the used computational grid

2.2. Boundary layer shielding

The simulations in the present work were performed with the BDES shielding model [16] combined with the shear layer adaptive filter width model Δ_{SLA} and the numerical parameters described in section 2.1. The BDES shielding function is shown in Fig. 2 in several chord-wise slices at different spanwise positions through the flow field at an angle of attack of α=12° on the wing's suction side. Three profiles of the shielding function $1 - f_d$ and the normalized streamwise velocity u/U_∞ at two spanwise positions are plotted on the right-hand side of the figure. When $1 - f_d =$

DOI: 10.13009/EUCASS2022-6085

1, the hybrid model operates in RANS mode, if $1 - f_d = 0$, LES mode is activated. Positions 1 and 2 in the region of attached flow show a shift of the RANS/LES interface further away from the wing surface with increasing chordwise position. Here, an overall satisfactory shielding of the attached boundary layer along the complete chord is clearly visible. At position 3 the profile is extracted directly downstream from the leading edge but upstream from the separation line. The boundary layer is also sufficiently shielded at this location.

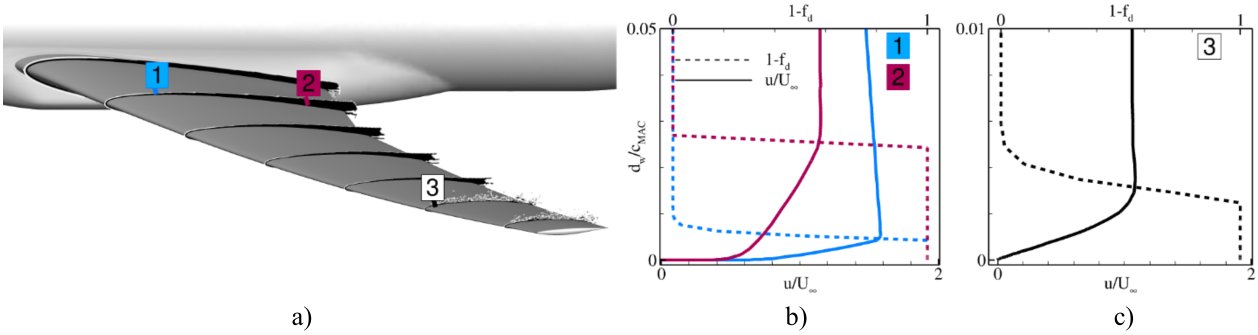

Figure 2: BDES shielding function on the wing's suction side. b): Position 1 and 2, c): Position 3.

3. Results

The present work provides a characterization and comparison of the beginning flow separation and the resulting wake at two angles of attack. First, a basic validation of the numerical results of lift, drag, and surface pressure coefficients is performed based on comparisons with wind tunnel data from the ESWI^{RP} campaign [3]. Then, an insight into the flow separation characteristics is given, Finally, the wake flow is investigated by means of first and second order flow statistics and spectral analyses.

3.1. Forces and pressure distributions

Figure 3 shows the lift and drag coefficients of the CRM as a function of the angle of attack as determined in the ESWI^{RP} campaign. Black squares show the simulated lift coefficient at α=12° and α=14°. Gray triangles the corresponding drag coefficients. The range of fluctuation of the simulated values is in the range of the symbol size. At α=12°, both the simulated lift and drag coefficients are very close to the experimental values, with lift only slightly underestimated and drag overestimated. At α=14°, the lift coefficient of the simulation is about 0.15 below the experimental value and the drag coefficient is overestimated by $\Delta C_D = 0.04$. However, it was observed that the drop of the lift coefficient visible in the experiment at α=16° occurred at different angles of attack between α=14° and 16° at different polar runs with the same flow conditions. This shows the high sensitivity of the present flow regime towards disturbances in the inflow. Therefore, the simulated result, which is at a lift level comparable to the level beyond the lift drop, can be considered reasonable.

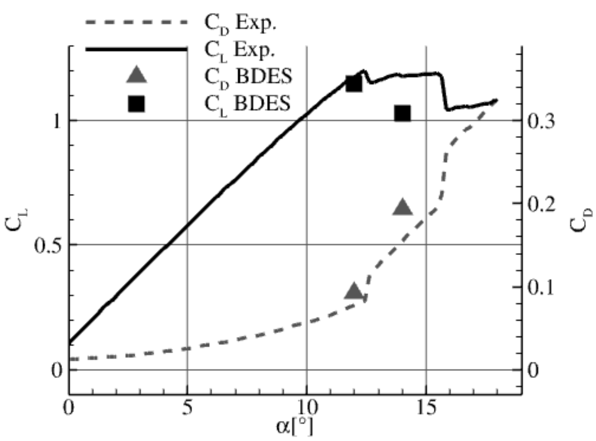

Figure 3: Lift and drag polar of the experiment and the simulated angles of attack

Figures 4 and 5 show the pressure distributions along the chord in three spanwise positions at 20%, 50% and 85% halfspan at the two investigated angles of attack. The triangles indicate the ESWI^{RP} pressure data. The black lines

DOI: 10.13009/EUCASS2022-6085

depict the time averaged pressure coefficient of the simulation. The standard deviation of c_p is shown using blue error bars.

At α=12°, shown in Figure 4, the two inboard positions yield excellent agreement between simulation and experiment. The smooth pressure distribution indicates fully attached flow. However, at the most outboard slice the sharp increase in pressure immediately downstream from the leading edge indicates flow separation in the simulation. This is also confirmed by the high pressure fluctuations that occur over the entire chord length. In contrast, the gradual increase in the experimental values suggests attached flow at this position. After approximately 30% chord length the simulated pressure distribution on the suction side follows the experimental pressure gradient and shows good agreement with the measured c_p.

The pressure distributions at the same slices are shown in Figure 5 at α=14°. An overall good agreement between simulation and experiment can be observed. In the most inboard slice, a continuous pressure increase with low pressure fluctuations occurs, which indicates attached flow. At the mid wing position a sharp suction peak followed by a constant pressure level from 5% chord length downstream to the trailing edge suggests flow separation directly behind the leading edge. The pressure fluctuations are slightly higher in the first 50% chord and decrease toward the trailing edge. This might be due to the increasing distance of the separated shear layer from the wing surface.

Outboard, a less sharp increase of pressure compared to the mid-wing section is followed by a small pressure gradient between 20% chord and the trailing edge in the experiment and the simulation. The simulation yields very high fluctuation values near the leading edge and still significant fluctuations throughout the entire chord. The measured static pressure distribution lies in the fluctuation range of the simulation. The fluctuations combined with the lack of pressure recovery at the trailing edge hint at separated flow over a large portion of the chord. Consequently, the separation is not triggered directly at the leading edge. This behavior might be due to the leading edge vortex curving back and leaving the wing surface, as described by Polhamus and Zhang et al.[7,8]. At the pressure side, the measurement and simulation yield a noticeable deviation at the most outboard slice. This may be due to the pressure taps being located at the opposite wing where a different and possibly asymmetric separation behavior might occur at this highly unstable flow regime. This behavior is also manifested in the measured rolling moment at these flow conditions which confirms the assumption of asymmetric flow separation.

All in all, the comparison of pressure distribution shows that the simulation can capture the different pressure distribution characteristics at the shown positions at 14°. At α=12°, the simulation seems to overestimate flow separation at the most outboard position. It shall be mentioned that as the flow is very sensitive in this flow regime, changes in the numerical parameters or deviations between the numerical and the experimental setup may have a noticeable impact on the results. Moreover, this is also valid for the numerical parameters, with remaining gray area and turbulence model influence among others. As the shown stall behavior agrees with the theory of swept wing stall and the results at α=14° show a very good agreement between simulation and experiment, we expect to capture the relevant effects of wing stall.

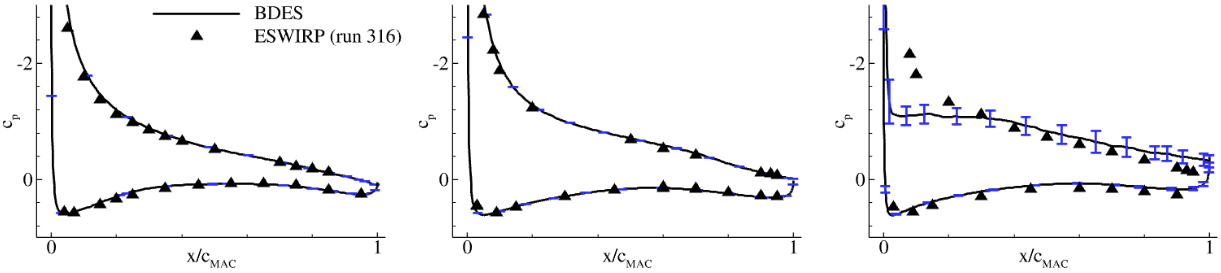

$a)\ \eta = 0.2$ b) $\eta = 0.5$ c) $\eta = 0.85$

Figure 4: Chordwise pressure distributions at three spanwise positions, α=12°, Blue errorbars denote $\pm\ c_{p,RMS}$

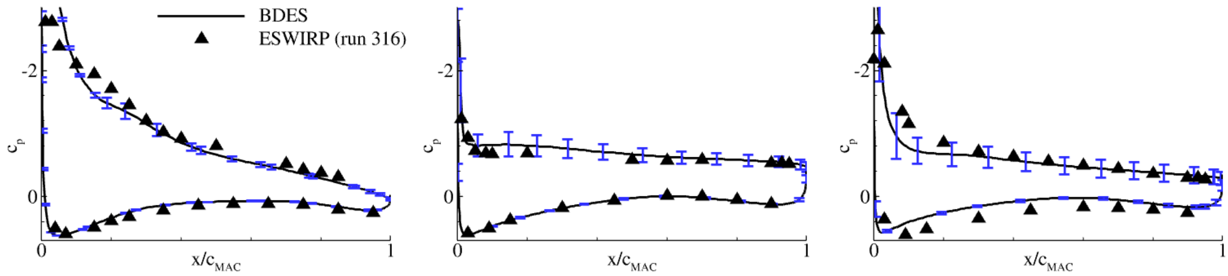

$a)\ \eta = 0.2$ b) $\eta = 0.5$ c) $\eta = 0.85$

Figure 5: Chordwise pressure distributions at three spanwise positions, α=14°. Blue error bars denote $\pm\ c_{p,RMS}$

DOI: 10.13009/EUCASS2022-6085

3.2. Flow Separation and Near-Wake Topology

From the measured pressure distributions at different spanwise positions, beginning stall can be identified in the outboard wing region, which rapidly expands inward with increasing α in a range between α =13° and α=15°. This behavior can also be observed in the simulation, with the onset of stall shifting to slightly lower angles of attack between α=11° and α=12°. At these angles of attack, the simulation shows flow separation directly at the leading edge at the outer wing section.

In order to gain a more detailed insight into the stall characteristics, Figure 6 shows the root mean square of the pressure coefficient on the wing suction side as well as time averaged wall streamlines for both investigated angles of attack. The streamlines are obtained by integrating the time averaged wall friction vector. At α=12°, the regularly aligned streamlines with no swirl and the low surface pressure fluctuation level both represent attached flow in the inboard region up to 73% halfspan. The streamline curvature towards the wing tip due to wing sweep and decreasing srteamwise wall shear stress toward the trailing edge is clearly visible in this area.

Based on the flow separation topology introduced by Tobak and Peake [23] the streamlines indicate a global line of separation in the vicinity of the leading edge, which is defined by converging streamlines from up- and downstream direction. At 93% halfspan, a saddle point can be observed from which the streamlines run outboard toward the tip and inboard toward a focus point of separation characterized by convergence of the skin friction lines towards a singular point at η=75%. The focus point, following the theory of Harper and Maki [6], can be interpreted as the position where the leading edge vortex rolls up and a distinct streamwise vortex leaves the wing surface, which might explain the vortical structure visible in the pattern of the wall streamlines. Flow recirculation and an increased level of pressure fluctuations indicate fully separated flow from the nodal point of separation towards the wing tip. At α=14°, the flow topology remains largely the same. However, the vortical structure of the streamline pattern has shifted further inboard and is located at η=25%. Moreover, the separation line is curved backwards toward the wing tip. This leads to streamlines that run in inflow direction downstream from the leading edge. A large recirculation area is present in the rear part of the wing. These observations align with the measured and simulated pressure distriutions which indicate partly attached flow in the vicinity of the leading edge in the most outboard position shown in Figure 5. The saddle point in the separation line that splits the recirculating flow in a region of outboard directed flow toward the tip and a region where the flow near the leading edge is directed inboard is located at 60% halfspan.

The pressure fluctuations are slightly increased at the higher angle of attack with maximum values near the leading edge in the ouboard wing section and in the vicinity of the vortex leaving the wing surface.

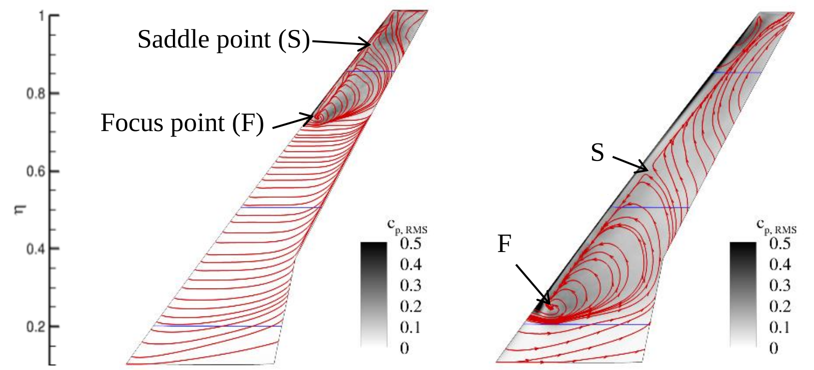

a) α=12° b) α=14°

Figure 6: Separation visualization by means of surface streamlines and root mean square of the pressure coefficient. Blue lines depict the positions of the pressure distributions shown in Figure 4 and 5.

In order to get an insight into the near wake topology, isosurfaces of $u/U_\infty = 0.5$ colored by spanwise velocity are illustrated for the two investigated angles of attack in Figure 7. At α=12° the upstream border of the isosurface is aligned parallel to the leading edge. It reaches its maximum spanwise extent near the leading edge where it spans from the vortical structure on the wing surface towards the wing tip. Downstream, above the trailing edge, the inner limit of the wake deficit has shifted outboard and the spanwise wake extend is decreased. The spanwise flow is directed inwards near the separation vortex resulting from the sense of rotation of the vortex. At α=14° the wake has become significantly larger in spanwise and streamwise direction. However, it is also limited inboard by the vortex detaching from the wing surface. Towards the wing tip, the upstream boundary of the isosurface shown also stretches backwards due to the curved separation line. The largest streamwise extent of the wake is reached downstream from the saddle point highlighted in Figure 6. This point also marks the border between inward flow toward the vortex position and outward flow toward the tip. Downstream from the saddle point, no spanwise flow can be observed in the shown wake part of the wake.

DOI: 10.13009/EUCASS2022-6085

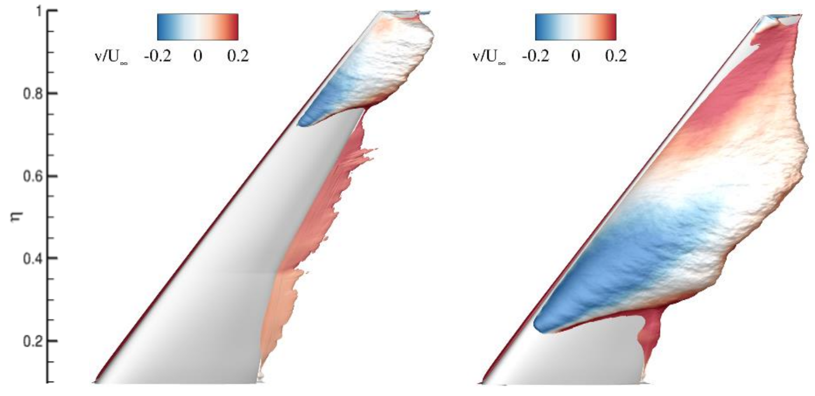

a) α=12° b) α=14°

Figure 7: Iso-surface of u/U_∞=0.5 colored by spanwise velocity

3.3. Wake Flow

The evolution of the streamwise vorticity in three wake slices is depicted in Figure 8 for both investigated angles of attack. Regions of low vorticity magnitude are blanked for clarity. Positive vorticity values denote counterclockwise rotation viewed from upstream. The extent of the velocity deficit in the wake is depicted by black isolines of u/U_∞=0.9. Besides high vorticity in the wing wake, vortical structures originating from the horseshoe vortex of the wing-fuselage-junction and a vortex emanating from the upper side of the fuselage can be observed. The influence of these vortices is not considered further in the present work, as its focus is on the separated wing wake.

At an angle of attack of α=12°, high streamwise vorticity can be observed in the outboard wing region in the most upstream plane. Maximum values can be found in the wake at the position of the wing tip vortex as well as slightly outboard from the position where the vortical structure could be observed in the wall streamlines. This vortex, which is supposed to be the leading edge vortex detaching from the wing surface, is termed inboard vortex in the following. Moving downstream, the propagation of these two vortices becomes clearly visible indicated by high vorticity values. The spanwise position of the vortices stays relatively stable, the wing tip vortex yields a slight upward shift in the wake. Due to the same sense of rotation of the inboard and wingtip vortex, respectively the separated wake develops an undulating shape with the highest point of the upper wake limit being located outboard of the inner vortex. In the third plane, the regions of high vorticity have become slightly blurred but are still clearly visible. Here, the velocity deficit is most pronounced in the vortex regions.

At α=14°, as shown in Figure 8b), the wing tip vortex and separation vortex induce distinct regions of high vorticity in the wake. While the evolution of the wing tip vortex agrees with the α=12° case, the inner vortex is located further inboard. Its spanwise position in the wake follows the position of the vortical structure shown in the wall streamlines in Figure 6. Compared to the lower angle of attack, the spanwise and vertical extent of high vorticity regions is increased. This leads to a more pronounced wavy shape of the wake with the maximum vertical wake extent being located outboard of the inner vortex. At the most downstream position, the separation vortex impinges on the tip region of the horizontal tailplane.

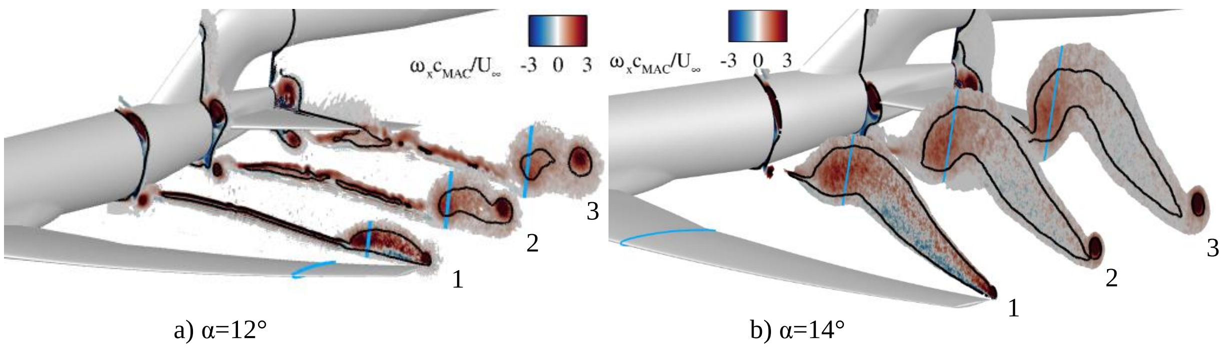

a) α=12° b) α=14°

Figure 8: Streamwise vorticity in the wake at three x-positions. Distance between the planes: $\frac{\Delta x}{MAC} = 1$

DOI: 10.13009/EUCASS2022-6085

A deeper insight into the wake turbulence statistics at the three streamwise planes depicted in Figure 8 is given in Figures 9-11 for both investigated angles of attack. The most upstream plane is shown at the top picture, the most downstream plane at the bottom picture, as indicated by the plane numbers in each figure. The gridlines shown at each plane are located at the same y and z coordinates, respectively for orientation. Contours of the mean spanwise velocity superimposed by streamwise velocity contour lines are depicted in Figure 9. The spanwise flow is directed inboard in the upper wake and outboard in the lower wake. This is consistent with the basic lifting line theory and contributes to the high positive streamwise vorticity in the wake shown in Figure 8. This behavior prevails downstream toward the tailplane. Regions of higher spanwise velocity magnitude can be observed in the regions of the wing tip vortex and the inboard vortex, respectively. These high velocity regions widen, the inboard vortex gets shifted downwards and the wing tip vortex upwards downstream in the wake. The spanwise vortex positions of the inboard vortices are shifted outboard compared to their position on the wing surface in Figure 6. At 12°, the vortex can be observed at approximately 85% halfspan and at α=14° it is located at approximately 40% halfspan. This is also consistent with the observations of Zhang et al.[10], where the vortices move outboard before they align parallel to the streamwise flow.
The lines of u/U_∞ show the evolution of the streamwise velocity deficit in the wake. At both angles of attack, the presence of the tip and inboard vortex lead to a wavy shape of the wake where the wake located between the two vortices gets shifted upwards. The velocity deficit shows the largest streamwise extent at the vortex cores, where energy from the inflow is transferred into spanwise and transversal velocity. Furthermore, in the wake center between 60 and 80% halfspan, a more pronounced velocity deficit can be observed at α=14° with outboard flow prevailing in this region. The regions of zero spanwise velocity widen downstream but stay fixed in space. They do not follow the wake deformation visible in the streamwise velocity deficit.

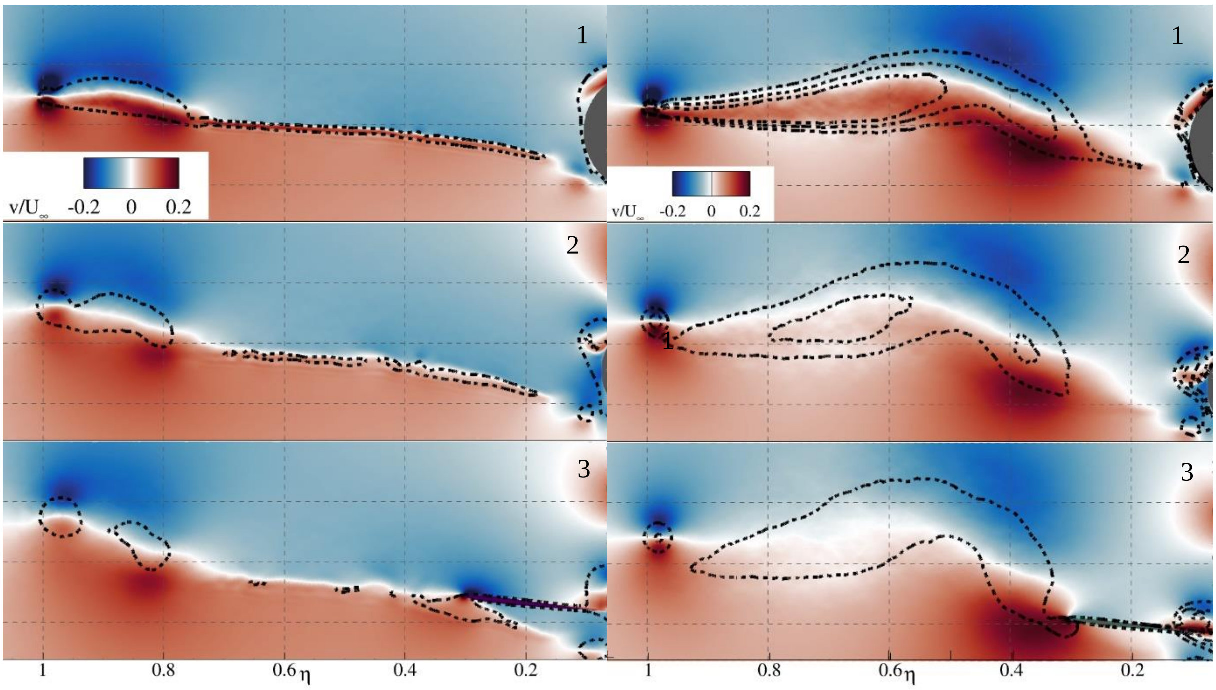

a) α=12°   b) α=14°

Figure 9: Mean spanwise velocity at three wake positions. View from downstream. Lines denote u/U_∞ =0.7,0.8,0.9

The transverse velocity component w, again with superimposed lines of the streamwise velocity deficit, is illustrated in Figure 10. Inboard wake regions downstream from attached wing flow domains show negative w-velocity resulting from the downwash generated by the wing. The positions of the two vortices are associated with areas of high w-velocity that dominate the transverse velocity distribution in the separated wake. Fluid from the lower part of the wake is pushed upwards outboard from the vortex core position of the inner vortex. Additionally, fluid is pushed downwards in the outboard wake region by the tip vortex. These 2 effects are the main drivers of the transversal movement in the separated wake. At α=14°, this leads to spanwise areas of downward and upward flow in the downstream wake planes. At α=12°, the effect is also present but less clearly visible due to interference of the two vortices that are located closer together. The region of the most distinct velocity deficit between the two vortices is located in regions of relatively low vertical movement. At both angles of attack the tailplane encounters downwash as the wing is not fully separated upstream of the tailplane. At α=14° the downwash is amplified by the presence of the inboard vortex which decreases the local angle of attack of the tailplane.

DOI: 10.13009/EUCASS2022-6085

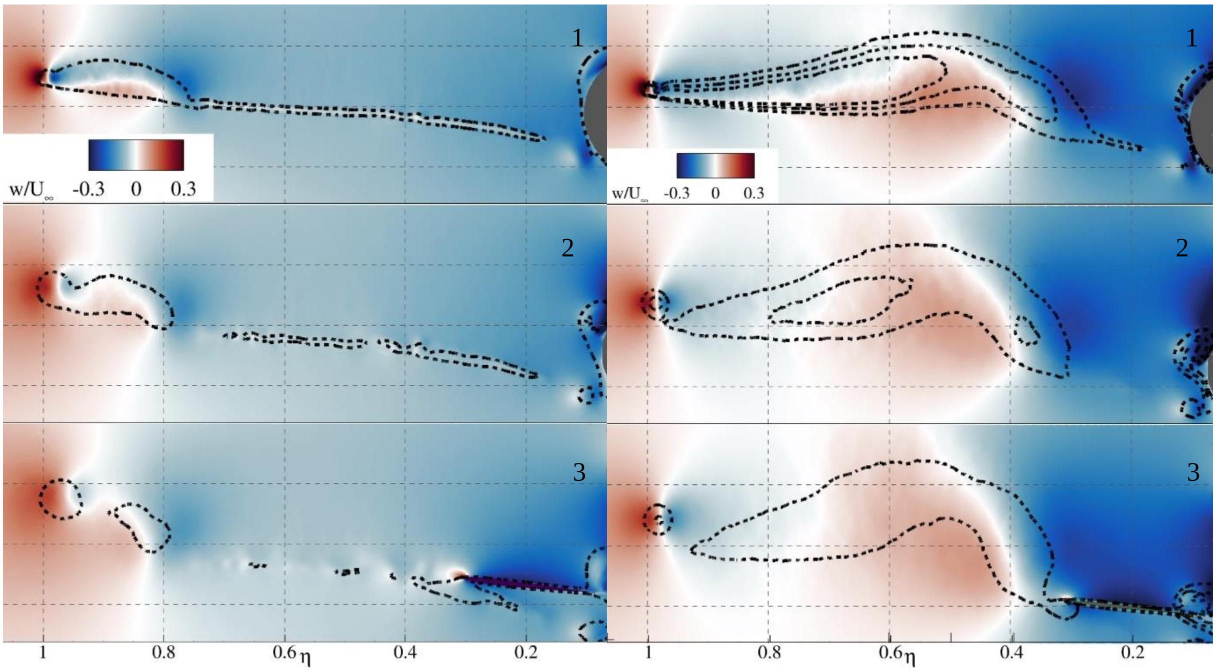

a) α=12° b) α=14°

Figure 10: Mean transverse velocity in three wake positions. Lines denote u/U_∞ =0.7,0.8,0.9

The turbulence kinetic energy k_t at the three streamwise planes shown in Figure 11 gives information about the turbulence and unsteady motion of the wake. The regions of high k_t basically follow the shape of the streamwise velocity deficit. High values of k_t are visible in the most upstream plane throughout the separated wake with slightly lower values at the inboard vortex positions. The magnitude of k_t significantly decreases downstream. Maxima can be observed in the wake center in vertical direction and especially in the wing tip vortex. While k_t is uniformly distributed in the wake at α=12°, minimum values occur in the outer wing region at α=14°. This may be connected to the flow not being fully separated in this spanwise domain and therefore less turbulent mixing occurs in the wake. In the most downstream plane, a region of unsteady inflow hits the tailplane tip at α=14° and therefore may induce unsteady loads.

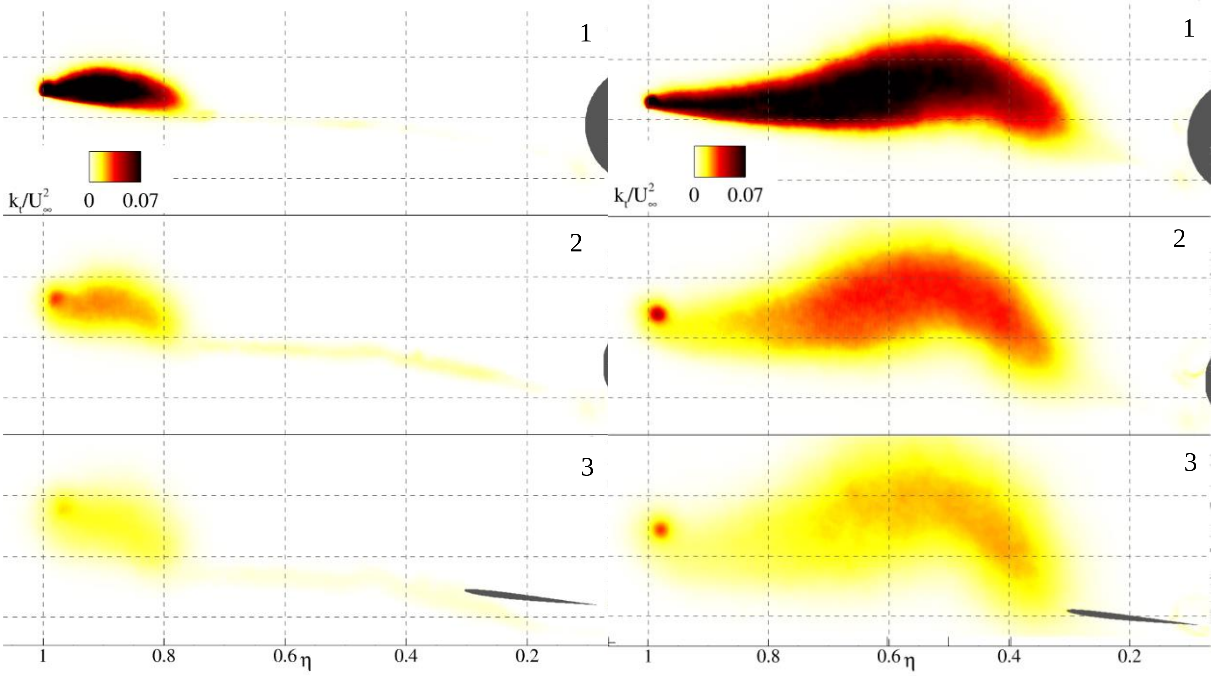

a) α=12° b) α=14°

Figure 11: Turbulence kinetic energy in three wake positions.

DOI: 10.13009/EUCASS2022-6085

In the Figures 12 to 14, vorticity and flow statistics in streamwise planes enable a deeper insight into the streamwise wake development. The two planes shown are located near the respective position where the inboard vortex leaves the wing surface for each angle of attack. Consequently, at α=12° a plane at η=85% is investigated, at α=14° the plane is located at η=28%. The position of the two planes is indicated by blue lines in Figure 6.
First, the normalized spanwise vorticity ω_y based on the velocity field at one point in time is depicted in Figure 12. Black lines depict the position of the streamwise planes of Figures 8-11. At both angles of attack, high vorticity is generated in the separation shear layer above the wing surface whose breakdown and interaction with the trailing edge shear layer leads to the characteristic large scale vortex shedding as described by Huang and Lin[5]. This meandering motion can be observed at both angles of attack. However, it is more pronounced at α=14°. In the vicinity of the leading edge, the shear layer shows a faster breakup into vortical structures at the higher angle of attack. Moreover, the vortices above the wing and in the wake are smaller in size compared to α=12°.

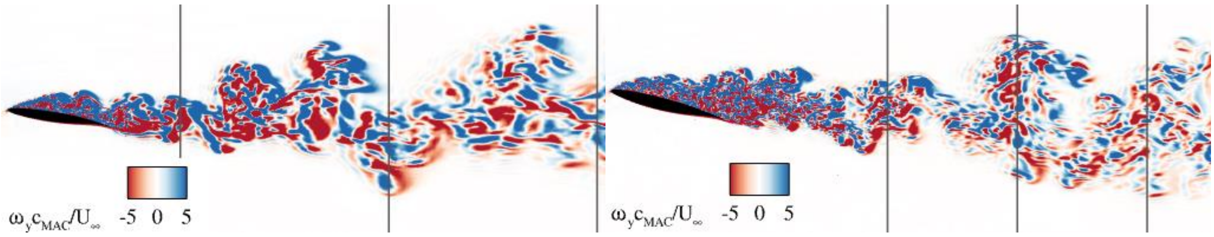

a) α=12°, η=85% b) α=14°, η=28.3%

Figure 12: Instantaneous spanwise vorticity at the respective spanwise positions of the inboard vortex

Figure 13 shows the time averaged streamwise and transverse velocities at the spanwise position of the separation vortex. White and blue lines depict u/U_∞ = 0 near the wing surface, u/U_∞ = 0.5 and u/U_∞ = 0.8, respectively. At α=12°, the recirculation zone is restricted to areas close to the wing surface and yields its largest vertical extent at approximately 50% local chord. At α=14°, the higher angle of attack leads to a larger recirculation area and a more pronounced velocity deficit in the wake. Furthermore, the wake is deflected further downwards than at α =12°.
The normalized transverse velocity w/U_∞ in the bottom row of Figure 13 yields a comparable topology at both angles of attack. Positive transverse velocity prevails in the recirculation regions above the wing surface and in the wake after the trailing edge shear layer has broken up. This is due to the influence of the inboard vortex, which induces upward flow behind the wing at this spanwise position. This characteristic region of upward directed flow is preserved downstream in the wake at both angles of attack. At α=14° the downward deflection of the region of positive w-velocity and thus the deflection of the inboard vortex is clearly visible. In contrast, the vertical position of the vortex stays constant at α=12°. In the upper wake, negative transverse velocity can be observed that reaches its maximum magnitude above the trailing edge.

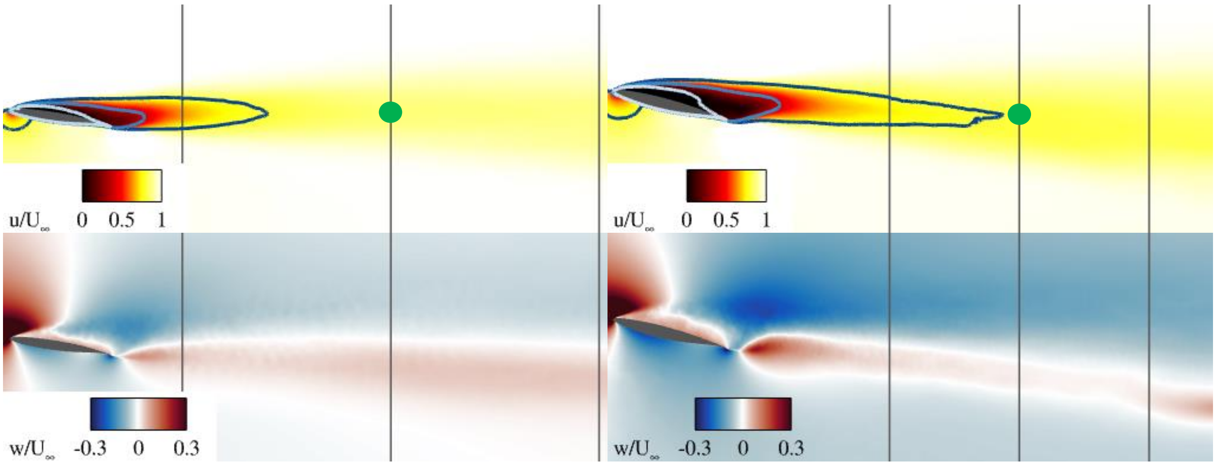

a) α=12°, η=85% b) α=14°, η=28.3%

Figure 13: Time averaged streamwise and transverse velocity at the respective spanwise positions of the inboard vortex. Green dots denote the positions of the point spectra in Figure 15. Lines denote u/U_∞ =0, 0.5, 0.8

DOI: 10.13009/EUCASS2022-6085

The turbulence kinetic energy k_t and the shear stress $\overline{u'w'}$ in streamwise slices between the wing and horizontal tailplane are depicted in Figure 14. At both angles of attack, k_t yields the highest values above the wing in the shear layer emanating from the leading edge. In the wake, a fast decay of k_t is visible with maximum values in the wake center. At α=14°, the shear layer and therefore the maximum of k_t is shifted further away from the wing surface, which can be attributed to the higher angle of attack. Near the upper wing surface, relatively low k_t occurs at α=14° compared to α=12°. The trailing edge shear layer at α=14° yields higher k_t values and therefore contributes to an elevated level of turbulence kinetic energy behind the trailing edge. Furthermore, the streamwise extent of high k_t is larger at α=14°.

The shear stress component $\overline{u'w'}$ can be interpreted as a measure for momentum exchange between free stream above the shear layer and the recirculating flow below it. Its magnitude is high in the shear layer region above the wing where it yields negative values. Fluid moving in positive z direction (w>0) from inside the recirculation region has very likely negative streamwise velocity (u<0) as it moves into a region of higher momentum. The opposite holds for the trailing edge shear layers, where $\overline{u'w'}$ yields high positive values. This characteristic is preserved downstream in the wake, where the shear layers widen up and $\overline{u'w'}$ decreases in magnitude. While both angles of attack yield comparable magnitudes of $\overline{u'w'}$ above the wing, its value in the trailing edge shear layer is weaker at α=12° which also yields a smaller vertical extent of high positive shear stress. Again, a stronger downward deflection of the wake at α=14° is visible.

High values of $\overline{u'w'}$ and k_t in the shear layer above the wing show that the velocity fluctuations are resolved immediately downstream from the separation position. This is a sign for the efficacy of the used gray area mitigation tools and therefore provides a good starting point for the investigation of turbulence downstream in the wake.

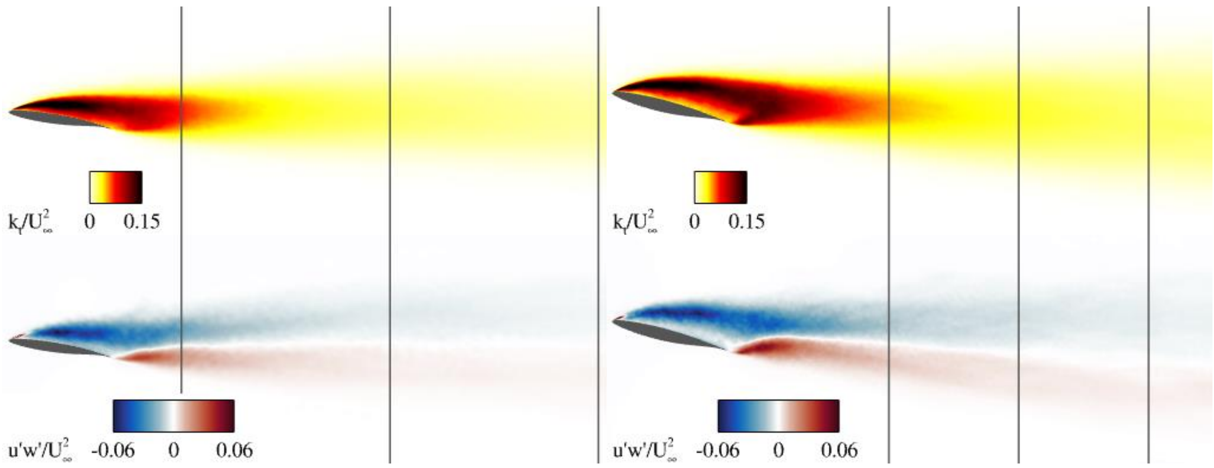

a) α=12°, η=85% b) α=14°, η=28.3%

Figure 14: Turbulence kinetic energy and shear stress $\overline{u'w'}$ at the respective spanwise positions of the inboard vortex

Spectra of the streamwise, spanwise and transverse velocity fluctuations in the wake center at the intermediate wake plane are illustrated in Figure 15 for both investigated angles of attack. The spectra were obtained with the Welch method with the signal being split into 6 bins. The time series used in the present work contains $100t_\infty$ and therefore results in a frequency resolution of $Sr_{MAC} \approx 0.01$. In order to ensure sufficient statistical convergence, the evaluation of flow dynamics that occur at lower frequencies than $Sr_{MAC} \approx 0.3$ will be part of future work, where a longer simulation time series will be investigated. The w-spectra are multiplied by a factor of 0.01, the v-spectra by a factor of 0.1 to enable a better distinction of the curves. The extraction points of the spectra are located at the respective wake center and indicated by green dots in Figure 13. Yarusevich and Boutilier [24] and Huang and Lin [5] showed similarities of the wake behind a stalled airfoil to the wake behind a bluff body with a characteristic von Kármán like vortex street. The spectral content of different bluff body wakes can be compared by using the projection of the body to a plane normal to the inflow direction as reference thickness d to obtain a Strouhal number Sr_d. The definition of d is illustrated in between the spectra of Figure 15. Yarusevich and Boutilier [24] and Roshko [25] yielded values in the range of Sr_d=0.2 for the dominant vortex shedding frequency of various bluff body wakes at high Reynolds numbers. Waldmann [1] demonstrated that this analogy can be expanded to the separated wing wake of the CRM in post stall at a similar frequency range.

At α=12° all three spectra reveal peaks at Sr_d=0.18. Those peaks in the u and w spectra may be attributed to the vortex shedding in the wake. However, this dominant frequency is also visible in the spanwise velocity spectrum. This hints at an interaction of the vortex shedding with the rotational flow around the inboard vortex. Therefore, a complex three-dimensional motion at the vortex shedding frequency takes place in the region of the vortex convecting downstream

DOI: 10.13009/EUCASS2022-6085

in the wake. Furthermore, a distinct low frequency peak at Sr_d=0.075 can be observed in the w-velocity spectrum. This might be connected to events of shear layer breakdown above the wing that lead to strong perturbations in the transverse velocity that propagate downstream in the wake.
At α=14° the u and w-spectra reveal similar dominant frequencies with a region of elevated PSD between Sr_d=0.18 and 0.22 which agrees well with the large-scale vortex shedding of a bluff body wake. The elevated PSD level at the vortex shedding frequency of the spanwise velocity indicates the same effect of three-dimensional motion at the vortex position as described at α=12°. Above $Sr_d = 0.22$ all three spectra show a continuous decay of PSD level toward higher frequencies.
The peak at the characteristic vortex shedding frequency range is less distinct at α=12° compared to α=14°, especially in the w-spectra revealing that the bluff body analogy might not be as clearly transferable to lower angles of attack as for the higher αs. This might be due to the weaker trailing edge shear layer and therefore the wake is primarily influenced by the leading edge shear layer.

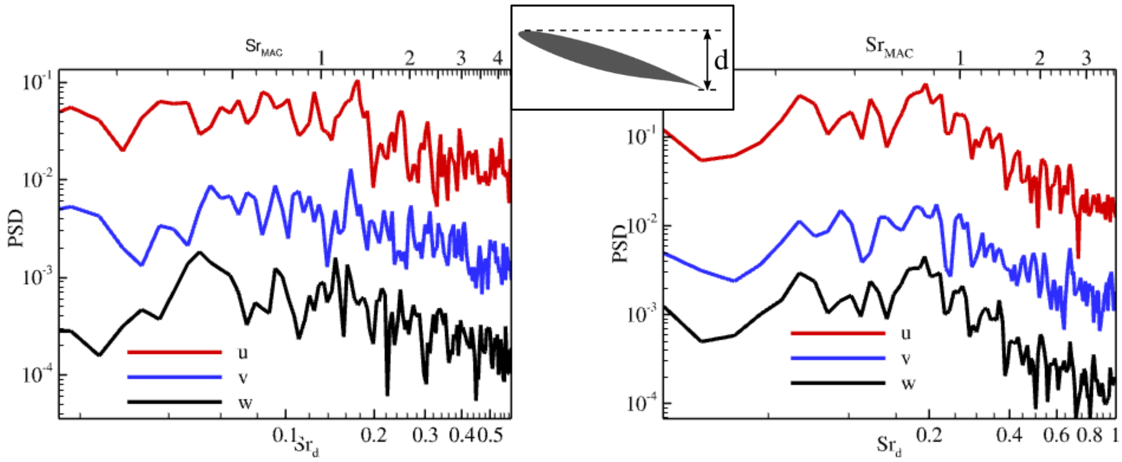

a) α=12° b) α=14°

Figure 15: Spectra of the wake turbulence at the position of the separation vortex in medium wake positions (see Figure 13 for positions)

4. Conclusions

In the present work, flow separation and wake of the NASA CRM at beginning stall was investigated. The numerical setup was validated against experimental data of the ESWI^{RP} campaign [3] and it was shown that the applied hybrid RANS/LES model in conjunction with effective gray area mitigation, enables to reproduce the onset of stall and the stall characteristics at the swept wing of a transport aircraft configuration. Furthermore, the analysis of flow statistics in the wake gave insight into the occurring flow physics and shed light into the development of wake turbulence at these flow conditions. It was shown that the wake flow is dominated by two streamwise vortices, the wing tip vortex and the inboard vortex that detaches from the wing surface and propagates downstream in the wake. The latter moves inboard with increasing angle of attack and shifts from 85% halfspan at α=12° to 40% halfspan at α =14°. The presence of both vortices that rotate in the same direction leads to an upward shift of the wake center that results in a spanwise deformation into an undulating, wavy shape. The investigation of spanwise planes revealed that resolved turbulence mainly originates from the leading edge and trailing edge shear layers and propagates downstream. In the wake, vortex shedding with a dimensionless frequency, comparable to the flow behind bluff bodies, could be observed. However, this effect is more distinct at the higher angle of attack. Due to the presence of the vortices the vortex shedding frequency transfers to the spanwise domain and reveals a three-dimensional motion in the wake near the downstream propagating inboard vortex. In order to give insight into the statistics of low frequency phenomena below Sr_{MAC}=0. 3 a longer time series will be investigated. Furthermore, more detailed flow investigations and modal analyses are part of future work. To conclude, the present work gives a deeper insight into the main flow dynamics that influence the wake under stall conditions. These insights enable a better understanding of the underlying flow phenomena at the borders of the flight envelope.

Acknowledgements
The work is funded by the Deutsche Forschungsgemeinschaft DFG (German Research Foundation) in the project LU 809/8. The authors gratefully acknowledge the High Performance Computing Center Stuttgart (HLRS) for providing the computational resources for the simulations that were performed on HPE Hawk. We would also like to thank DLR for providing the TAU source code.

DOI: 10.13009/EUCASS2022-6085

References

[1] Waldmann, A., Lutz, T., and Kraemer, E. „Separated Wake Flow and Tail Loads of the Common Research Model in Low Speed Stall Conditions." In AIAA Scitech 2019 Forum, 2019, p. 2315

[2] Waldmann, A., Lutz, T., and Krämer, E., "Unsteady Simulation of a Separated Wake of a Transport Aircraft by Detached Eddy Simulation," New Results in Numerical and Experimental Fluid Mechanics XI, Springer International Publishing, Cham, 2017, pp. 61–71.

[3] Lutz, T., Gansel, P.P., Waldmann, A., Zimmermann, D.M. and Schulte am Hülse, S.A. "Time-resolved prediction and measurement of the wake past the CRM at high Reynolds number stall conditions." Journal of Aircraft **53**(2), 501–514, 2016. https://doi.org/10.2514/1.C033351

[4] Vassberg, J.C., DeHaan, M.A., Rivers, M.B. and Wahls, R.A.: "Development of a Common Research Model for Applied CFD Validation Studies" AIAA 2008-6919, 2008, https://doi.org/10.2514/6.2008-6919,

[5] Huang, R.F. and Lin, C.L.: "Vortex Shedding and Shear-Layer Instability of Wing at Low Reynolds Numbers." AIAA Journal 33(8), 1995, 1398–1403

[6] Harper, C. W., and Maki, R. L. "A Review of the Stall Characteristics of Swept Wings." NASA Technical Note TN D-2373, 1964.

[7] E. C. Polhamus. "A Survey of Reynolds Number and Wing Geometry Eects on Lift Characteristics in the Low Speed Stall Region." Technical Report CR-4745, NASA, 1996.

[8] Zhang, K., Hayostek, S., Amitay, M., Burtsev, A., Theofilis, V., and Taira, K. "Laminar separated flows over finite-aspect-ratio swept wings." Journal of Fluid Mechanics, 2020, 905.

[9] Ehrle, A.M., Waldmann, A., Lutz, T., and Krämer, E.: "Flow Separation and Wake of the Common Research Model at Low Mach Numbers". Proc. AVT-307 Research Symposium, Trondheim, 2019

[10] Spalart, P.R., Deck, S., Shur, M.L., Squires, K.D., Strelets, M.K. and Travin, A.: "A New Version of Detached-Eddy Simulation, Resistant to Ambiguous Grid Densities." Theoretical and Computational Fluid Dynamics20(3), 181–195, 2006

[11] Shur, M. L., Spalart, P. R., Strelets, M. K., and Travin, A. K. "A Hybrid RANS-LES Approach with Delayed-DES and Wall-modelled LES Capabilities." International Journal of Heat and Fluid Flow, 29(6), 2008, 1638-1649.

[12] Ashton, N., West, A., Lardeau, S., and Revell, A., "Assessment of RANS and DES Methods for Realistic Automotive Models." Computers and Fluids, Vol. 128, 2016, pp. 1–15.

[13] Shur, M. L., Spalart, P. R., Strelets, M. K., and Travin, A. K., "An enhanced version of DES with rapid transition from RANS to LES in separated flows," Flow, turbulence and combustion, Vol. 95, No. 4, 2015, pp. 709–737

[14] Mockett, C., Fuchs, M., Garbaruk, A., Shur, M., Spalart, P., Strelets, M., Thiele, F. and Travin, A.: "Two Non-Zonal Approaches to Accelerate RANS to LES Transition of Free Shear Layers in DES." In: Girimaji, S., Haase, W., Peng, S.H., Schwamborn, D. (eds.) Progress in Hybrid RANS–LES Modelling. Notes on Numerical Fluid Mechanics and Multidisciplinary Design, vol. 130, pp.187–201. Springer, 2015

[15] Ehrle, M.C., Waldmann, A., Lutz, T. and Krämer, E. "An Automated Zonal Detached Eddy Simulation Method for Transonic Buffet." In: Hoarau, Y., Peng, SH., Schwamborn, D., Revell, A., Mockett, C. (eds) Progress in Hybrid RANS-LES Modelling. Notes on Numerical Fluid Mechanics and Multidisciplinary Design, vol 143. Springer, Cham. ,2020, https://doi.org/10.1007/978-3-030-27607-2_22

[16] Weihing, P., Letzgus, J., Lutz, T., and Krämer, E., "Development of alternative shielding functions for dηched-eddy simulations," Progress in Hybrid RANS-LES Modelling, contributions to the 7th Symposium on Hybrid RANS-LES Methods, Berlin 2018, p. 109-118. https://doi.org/10.1007/978-3-030-27607-2_8

[17] Schwamborn, D., Gerhold, T. and Heinrich, R.: "The DLR TAU-Code, Recent Applications in Research and Industry." European Conference on Computational Fluid Dynamics ECCOMAS CFD 2006

[18] Spalart, P. R., and Streett, C., "Young-person's guide to detached-eddy simulation grids," Tech. rep., NASA CR-2001-211032, 2001

[19] Löwe, J., Probst, A., Knopp, T., and Kessler, R., "Low-Dissipation Low-Dispersion Second-Order Scheme for Unstructured Finite Volume Flow Solvers," AIAA Journal, Vol. 54, No. 10, 2016, pp. 2961–297

[20] Travin, A., Shur, M., Strelets, M., and Spalart, P., "Physical and numerical upgrades in the detached-eddy simulation of complex turbulent flows," Advances in LES of complex flows, Springer, 2002, pp. 239–254

[21] Spalart, P. and Allmaras, S. "A one-equation turbulence model for aerodynamic flows". In 30th aerospace sciences meeting and exhibit 1992 (p. 439).

DOI: 10.13009/EUCASS2022-6085

[22] Ehrle, M., Waldmann, A., and Lutz, T. "Influence of the Wind Tunnel Model Mounting on the Wake Evolution of the Common Research Model in Post Stall". In STAB/DGLR Symposium 2020 (pp. 3-13). Springer, Cham.

[23] Tobak, M., and Peake, D. J. „Topology of three-dimensional separated flows." Annual review of fluid mechanics, 14(1), 61-85, 1982

[24] Yarusevych, S., Kawall, J. G., and Sullivan, P. E., "Separated-shear-layer development on an airfoil at low Reynolds numbers," AIAA journal, Vol. 46, No. 12, 2008, pp. 3060–3069.

[25] Roshko, A., "On the Wake and Drag of Bluff Bodies," Journal of the Aeronautical Sciences, Vol. 22, No. 2, 1955, pp. 124–132.672 https://doi.org/10.2514/8.3286